Microstructural evolution of helium-implanted α-SiC

J. Chen, P. Jung, and H. Trinkaus
Institut für Festkörperforschung, Forschungszentrum Jülich, D-52425 Jülich, Association EURATOM-FzJ, Germany
(Received 21 June 1999)

Helium has a decisive effect on the microstructure of silicon carbide materials after implantation and subsequent annealing. A dense population of bubbles and dislocation loops is already observed at relatively low displacement doses after annealing of helium-implanted α-SiC, while no visible damage appears after irradiation without helium implantation under otherwise equal conditions. The defects are separated from grain boundaries by defect-free zones of approximately 0.5 μm width. The most intriguing features of the evolving microstructure are lenticular cavities (platelets), which transform to disk-shaped arrangements of bubbles with associated dislocation loops or even stacks of loops. The observed microstructural evolution and its dependence on implantation dose, annealing temperature, and time are quantitatively explained and discussed in terms of diffusion of interstitial He atoms and their clustering between adjacent lattice planes, thus forming nanocracks during implantation. The relaxation of the high gas pressure by matrix atom transfer from bubbles to loops during annealing and the coarsening of bubble-loop complexes are described by a coupled two-component Ostwald ripening process.

I. INTRODUCTION

Interest in SiC extends from its application as a wide-band-gap semiconductor at high temperatures to its potential as a low-activation structural material in future fusion reactors. In the latter case helium is produced by nuclear transmutations while in semiconductors introduction of helium is proposed for gettering impurities. Previous investigations on helium-induced microstructural changes in SiC were confined to either shallow implantation of helium ions in the keV range[1–3] or neutron irradiation of boron-doped material.[4–9] In the present work, α particles with energies from 0 to $\approx$25 MeV were implanted homogeneously up to depths of mostly $\approx$100 μm. Therefore the results are not affected by surfaces (from shallow implantation) or grain boundaries (from boron segregation). After investigations of the effect of helium on dimensional changes[10] and fracture strength[11] of SiC-based materials, the present work gives a detailed and systematic account of the microstructural evolution after helium implantation and subsequent annealing.

II. EXPERIMENTAL DETAILS

Hot-pressed SiC of $\approx$98.5% purity and 3.2 g/cm^3 density was supplied in sheets of $\approx$350 μm by Elektroschmelzwerk Kempten. X-ray analysis gave 80% 6*H*-SiC, 18% 4*H*-SiC, and $\approx$2% free carbon, while transmission electron microscopy (TEM) in addition revealed small amounts of 3*C*-SiC (β-SiC) and 15*R*-SiC. These polytypes are well established in SiC and can be considered as a superstructure in the stacking along the *c* axis of a basic hexagonal lattice.[12,13] The sizes of 6*H* grains ranged from 1 to 5 μm, while some of the 4*H* grains had a rod-shaped appearance with lengths up to 30 μm. The grain structure of the material was stable up to the highest annealing temperature used (2120 K). The dominant defects in the material were stacking faults (SFs) on the (0001) planes with associated partial dislocations, and some black and white dots. These dots grew from $\approx$6 nm during thermal annealing at 1720 K to $\approx$10 nm, with no further change at 1920 K. Their nature could not be identified, as they showed no loop contrast under two-beam imaging and no additional diffraction pattern.

Helium implantation was performed at room temperature at the Compact Cyclotron of Forschungszentrum Jülich with a 26.3 MeV α beam which was scanned horizontally and vertically for lateral homogeneity and passed through a 28 μm Al window into a vacuum chamber ($\leqslant 10^{-3}$ Pa). In front of the specimens was a degrader wheel with 51 aluminum foils of appropriate thickness to give a homogeneous distribution up to a maximum depth that could be adjusted from 100 to 200 μm. The beam current was measured electrically on the insulated specimen holder. Specimens were fixed with Wood's metal to a copper heat sink, ensuring maximum temperatures of $\leqslant$350 K during implantation and unmounting. Average numbers of displaced atoms produced in SiC per implanted helium atom range from $\approx$60 for the maximum implantation depth of 100 μm to $\approx$73 for 200 μm. For details of the calculation, compare Ref. 14. Monte Carlo calculations[15] by TRIM95 give higher values by about a factor of 1.6.

The specimens were annealed by dropping into a hot tungsten tube furnace in a vacuum $\leqslant 10^{-4}$ Pa. Heating time was estimated to a few seconds and typical initial cooling rates after switching off the heating were 40 and 700 K/s at 1000 and 2000 K, respectively. After annealing, specimens were thinned from both sides by dimpling and subsequent ion milling (Gatan 691 PIPS) for TEM investigations (Philips TEM430, 300 kV). The main TEM techniques employed were phase contrast for identification of small bubbles and weak-beam imaging and the inside-outside method to determine the nature and Burgers vectors of loops. The size of cavities with diameters larger than 2 nm was determined from the inner bright area of the underfocused image. Foil thicknesses needed for density measurements were determined from the width of SF's as a function of tilting angle, and if no SF's were available from calibrated x-ray fluorescence.[16] For more experimental details, see Ref. 17.

TABLE I. Microstructural evolution of helium-implanted α-SiC as a function of helium concentration c_{He} (at. ppm) and annealing temperature T_a for an annealing time of 1 h. Symbols used:–, not investigated; GB, grain boundary; GI, grain interior (matrix); ∅, no visible defects; *s-c*, strain contrast; *P*, platelets (''two-dimensional'' bubbles); *B*, bubbles; *B*-disk, bubble disk; *B*-rod, rod-shaped bubbles, i.e., interconnected bubbles; *L*, dislocation loops; and *L*-stack, stacks of loops.

		C_{He}				
T_a (K)	C_{He}	200	350	600	1500	2450
⩽350	GB	–	–	∅	∅	*s-c*
	GI	–	–	∅	∅	*P*
1120	GB	–	–	∅	–	*s-c*
	GI	–	–	∅	–	*P*
1320	GB	–	–	∅	–	–
	GI	–	–	∅	–	–
1520	GB	–	*B*	*B*	–	*B*
	GI	–	*P*,*B*,*L*-stack	*P*,*B*-disk,*L*-stack	–	*P*,*B*-disk,*L*-stack
1620	GB	–	–	*B*	–	–
GI	–	–	*B*,*L*	–	–	
1720	GB	*B*	*B*	*B*	*B*	*B*
	GI	–	*B*-disk,*L*-stack	*B*-disk,*L*,*L*-stack	*B*-disk,*L*	*B*-disk,*L*
1920	GB	–	–	*B*	–	–
	GI	–	–	*B*-disk,*L*	–	–
2020	GB	–	–	*B*-rod	–	–
GI	–	–	*B*-disk,*L*	–	–	–
2120	GB	–	–	*B*-rod	–	–
	GI	–	–	*B*,*L*	–	–

III. RESULTS

Table I gives an overview of the microstructural evolution in the grain boundaries (GB's) and the grain interior (GI) of α-SiC as a function of implantation dose and annealing temperature.

A. Grain boundaries

After room-temperature implantation up to 1500 at. ppm He, no defects were visible in grain boundaries, while at 2450 at. ppm some strain contrast appeared. The contrast was enhanced after annealing at 1120 K, but faceted bubbles appeared only at 1520 K. At lower doses also (the lowest concentration investigated was 194 at. ppm), bubbles at GB's appeared above 1520 K. With increasing temperature the bubbles at GB's grew and their number density decreased. Above ≈1720 K these bubbles coalesced to rod-shaped cavities, which around 2120 K exceeded the thickness of the TEM foils. A quantitative analysis of bubble evolution at GB's was difficult because of the dependence of bubble growth on the orientation of the adjacent grains. The dependence of bubble morphology on grain orientation is clearly seen in Fig. 1, which also shows that bubble growth was enhanced with increasing inclination of adjacent (0001) planes.

Bubbles at the GB's and in the grain interior were well separated by defect-free zones (DZ's), the widths of which depended on helium concentration and annealing conditions, but also on the orientation of the GB, mainly on its inclination to the (0001) plane. The smallest width was obtained for GB's parallel to (0001), i.e., corresponding to the smallest size of GB bubbles. Results for this case are given quantitatively in Fig. 2. Due to the existence of DZ's no bubbles were observed inside grains of diameter less than 0.5 μm.

B. Grain interior

As in the boundaries, no visible defects were observed in the grain interior after implantation up to 1500 at. ppm He. On the other hand, after implantation to 2450 at. ppm, 4*H*- and 6*H*-SiC grains showed strong strain contrasts of disk-shaped appearance, lying on (0001) planes. By through-focal bright-field imaging (Fig. 3), it was determined that the underlying defect is of cavity type (platelets), while dislocation loops could be ruled out. For more details, see Ref. 17. The

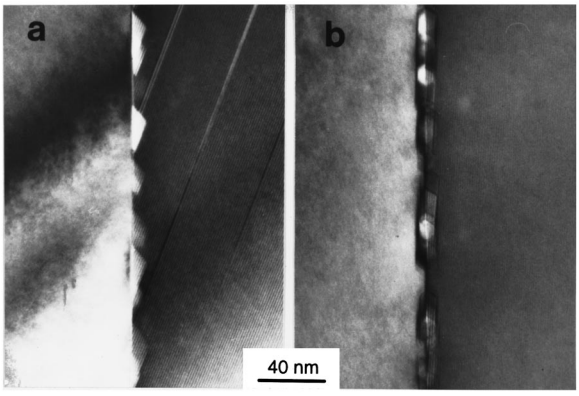

FIG. 1. Dependence of the morphology of GB bubbles on grain orientation in a specimen with 600 at. ppm He, annealed for 0.28 h at 1720 K. In both (a) and (b) the left-hand side grain has (0001) planes parallel to the GB, while in the right-hand side grains the (0001) planes are inclined by 20° (a) and 3° (b), respectively.

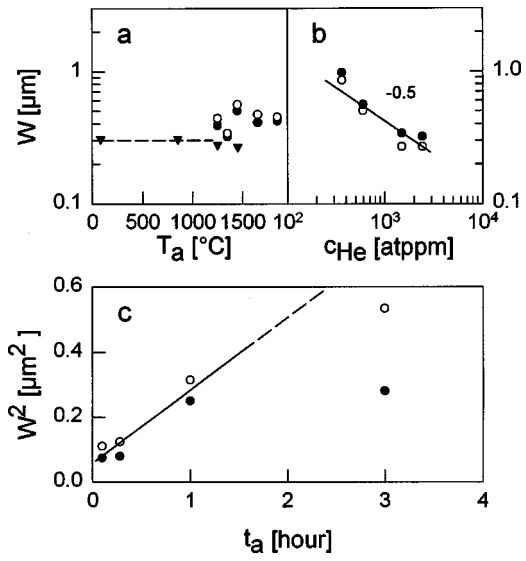

FIG. 2. Dependences of the width W of defect-free zones along grain boundaries parallel to (0001) planes in SiC on (a) annealing temperature T_a [$c_{\mathrm{He}}=600$ (○,●) and 2450 (▼) at. ppm, $t_a=1$ h], (b) helium concentration c_{He} ($T_a=1720$ K, $t_a=1$ h), and (c) annealing time t_a ($T_a=1720$ K, $c_{\mathrm{He}}=600$ at. ppm). Filled and open symbols indicate grains of 4H- and 6H-SiC, respectively.

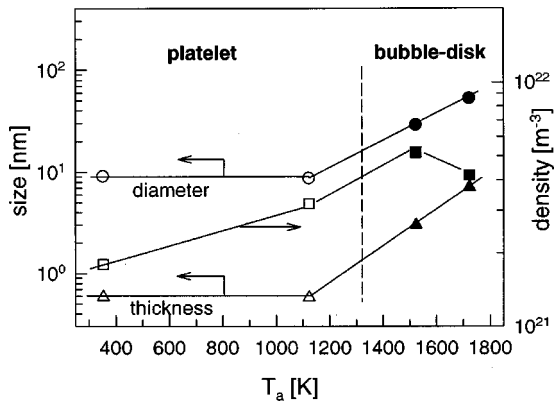

FIG. 4. Average diameters (○, ●), thicknesses (△, ▲), and number densities (□, ■) of platelets (open symbols) and evolving bubbles or bubble disks (filled symbols) in 4H-SiC grains, implanted to 2450 at. ppm He as a function of annealing temperature ($t_a=1$ h).

sizes and densities of platelets as a function of annealing temperature are shown in Fig. 4. Up to 1120 K the platelets did not grow, but only increased in number density. The size distribution of the platelets was found to be astonishingly narrow, with an average diameter of about 9 nm and an opening of about 0.6 nm. Somewhere between 1120 and 1520 K, a transition from platelets to disks of bubbles occurred with subsequent growth in size and decrease of number density.

At lower helium concentrations, such platelet-type contrasts were also observed but only after annealing above 1520 K. In this case, other defects became visible almost concurrently, namely, small bubbles, disks of bubbles, and associated dislocation loops. Various defect configurations evolving after annealing at 1720 K are shown in Fig. 5. Under the imaging conditions in this figure, cavity-type defects have good contrast, while loop-type defects give only weak contrast. Four major types of cavity-loop complexes can be distinguished: (I) A single bubble on the rim of a single loop; (II) a disk of bubbles with a single loop; (III) a disk of bubbles with small bubbles in the middle and larger ones on the rim of attached double or even multiple loops; (IV) a disk of bubbles with a large bubble in the center surrounded by small ones, associated with a stack of loops. Most complexes lay on (0001) planes, and their diameters are typically 35 nm (I), 70 nm (II), 150 nm (III), and 220 nm (IV). Type-IV complexes only appeared in a parameter window $c_{\mathrm{He}}\approx 350-600$ at. ppm, $T_a\approx 1720$ K, and $t_a\geqslant 1$ h. In this window some intersecting complexes were also observed, when some complexes lay also on the $(2\underline{1}\,\underline{1}0)$ or $(01\underline{1}0)$ planes. Type-IV complexes were not observed at the border of the DZ, but only further inside the grains (see Fig. 6). The parametric dependencies of the distributions of small and large bubbles evolving during annealing around 1720 K are given in Fig. 7. Annealing at 2120 K gave a coarsening of the bubble distribution, but the very large bubbles, which were typical for type-IV complexes, no longer formed and the other bubbles lost the connection with their loops.

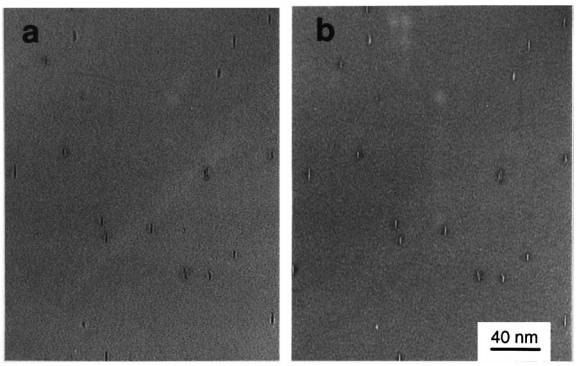

FIG. 3. Kinematic bright-field images of a 4H-SiC grain with 2450 at. ppm He, showing cavity-type platelets (edge on). (a) is under- and (b) overfocused. In both images the direction of the electron beam is close to $[01\underline{1}0]$.

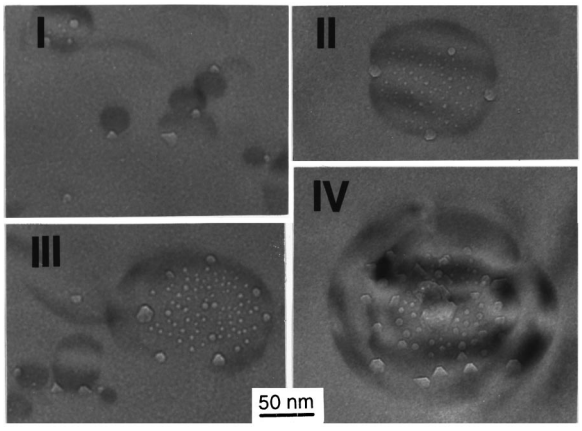

FIG. 5. Kinematic underfocused bright-field images of four different bubble-loop complexes in a 4H-SiC grain with 600 at. ppm He annealed for 1 h at 1720 K. (I) single bubble with single loop, (II) bubble disk with single loop, (III) bubble disk with double loop, and (IV) bubble disk with stack of loops. The direction of the electron beam was [0001].

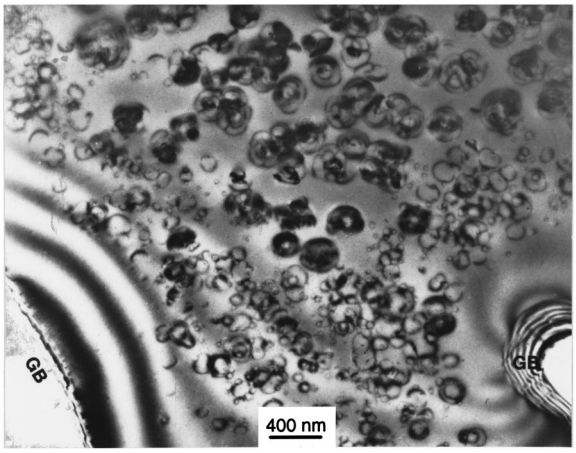

FIG. 6. Grain boundaries in 4*H*-SiC, implanted with 600 at. ppm He and annealed for 3 h at 1720 K. Along the DZ's a high density of single loops is observed, while in the center of the grain stacks of loops of lower density predominate. Beam direction was [0001].

All bubbles were faceted, with facets on (0001) and $(01\underline{1}2)$ planes in 4*H*-SiC and (0001) and $(01\underline{1}3)$ planes in 6*H*-SiC. Facets preferentially on close-packed planes were also found on voids in β-SiC.[18] Figure 8 shows that in a single grain all tips of the bubble ''pyramids'' (probably the growth direction) are oriented in the same direction. In Fig. 9 volume fractions of bubbles derived from diameters and number densities are shown. Obviously, $\Delta V/V$ increases with helium content and annealing temperature, but is almost independent of annealing time. These results are subject to some statistical uncertainties due to the dependence of bubble parameters on the distance from the DZ and because the position where the TEM picture was taken could not be exactly determined in all cases with respect to DZ's.

As already mentioned, bubbles were always accompanied by faulted dislocation loops of interstitial type. Most of them were on (0001) habit planes with Burgers vectors $\frac{1}{4}$ and $\frac{1}{6}$ of

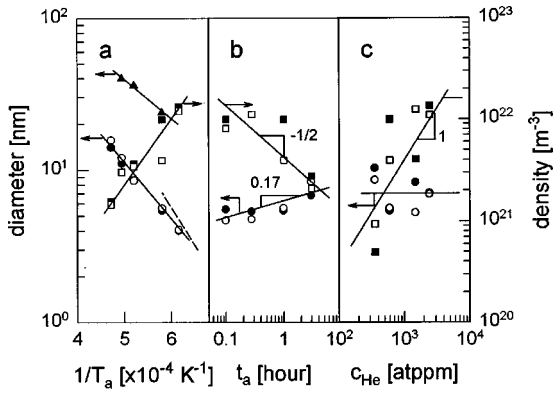

FIG. 7. Dependences of average diameters of small (○, ●) and large (▲) bubbles and bubble number densities (□, ■) on (a) annealing temperature T_a ($c_{\mathrm{He}}=600$ at. ppm, $t_a=1$ h), (b) annealing time t_a ($c_{\mathrm{He}}=600$ at. ppm, $T_a=1720$ K), and (c) He concentration c_{He} ($T_a=1720$ K, $t_a=1$ h). Filled and open symbols indicate 4*H*- and 6*H*-SiC grains, respectively. Solid lines are added to guide the eye and the dashed line in (a) gives thicknesses of the platelets in the 2450 at. ppm specimen (Fig. 4).

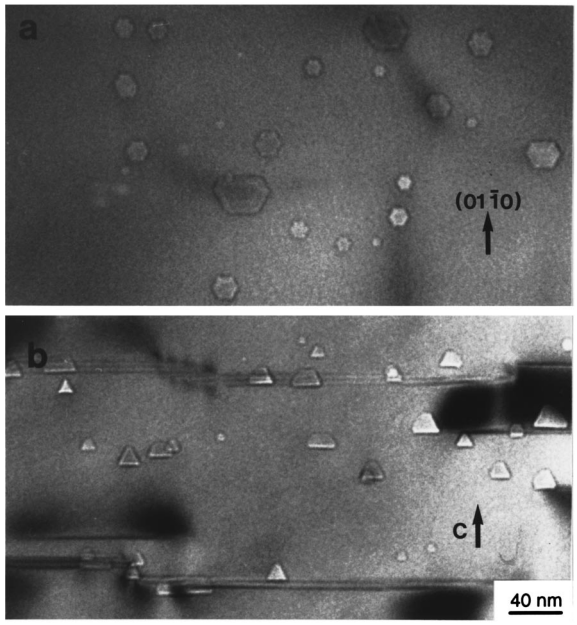

FIG. 8. Kinematic underfocused bright-field images of a 4*H*-SiC grain with 600 at. ppm He, annealed for 1 h at 2020 K. The direction of the electron beam was [0001] (a) and $[2\underline{1}\underline{1}0]$ (b), respectively.

[0001] in 4*H*- and 6*H*-SiC, respectively. Only a few percent were on $(2\underline{1}\,\underline{1}0)$ or $(01\underline{1}0)$ habit planes. The vertical extension of the above-mentioned type-IV complexes can be roughly estimated to about 10 nm. At 1920 K the stacks of loops had disappeared and only large single loops remained. The dependencies of loops and stacks of loops are summarized in Fig. 10. The sizes of single loops increase with temperature and time but are independent of helium concentration, while the diameters of the stacks of loops, which appear only in a narrow temperature window (see above), depend on neither time nor concentration. The number densities decrease with t_a and increase with c_{He}, respectively. Only number densities of complexes, i.e., of single loops plus stacks, are given as the number of individual loops in larger

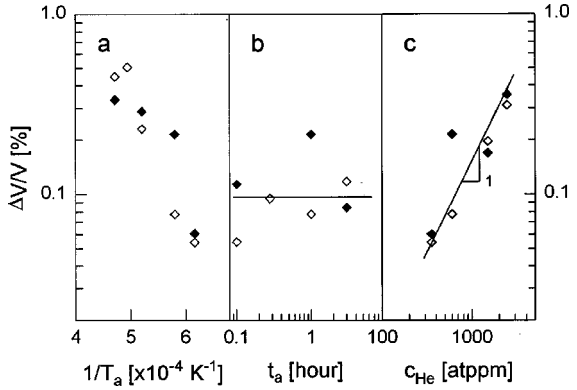

FIG. 9. Relative volume fraction of bubbles in 4*H*- (◆) and 6*H*-(◇) grains of SiC as a function of (a) annealing temperature T_a ($c_{\mathrm{He}}=600$ at. ppm, $t_a=1$ h), (b) annealing time t_a ($c_{\mathrm{He}}=600$ at. ppm, $T_a=1720$ K), and (c) He concentration c_{He} ($T_a=1720$ K, $t_a=1$ h). The solid lines roughly correspond to the lines in Fig. 7.

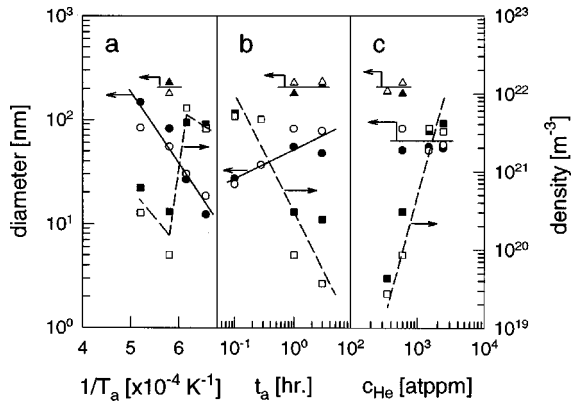

FIG. 10. Dependence of average diameters of single loops (○, ●), stacks of loops (△, ▲), and number densities of complexes (□, ■) on (a) annealing temperature T_a ($c_{\mathrm{He}}=600$ at. ppm, $t_a=1$ h), (b) annealing time t_a ($c_{\mathrm{He}}=600$ at. ppm, $T_a=1720$ K), and (c) He concentration c_{He} ($T_a=1720$ K, $t_a=1$ h). Filled and open symbols indicate 4*H*- and 6*H*-SiC grains, respectively. Lines are added to guide the eye.

stacks could not be precisely determined (cf. Fig. 5). This means that in the regime of stack appearance the given numbers underestimate the total number of loops. For example, the sharp drop of number density with increasing temperature in Fig. 10(a) reflects this problem of statistics. In Fig. 11(a) the total volume V_B of bubbles in a complex is given as a function of the total area A_L of the associated loop or double loops, while Fig. 11(b) gives the ratios of total bubble volumes to total loop areas in a specimen as a function of He concentration.

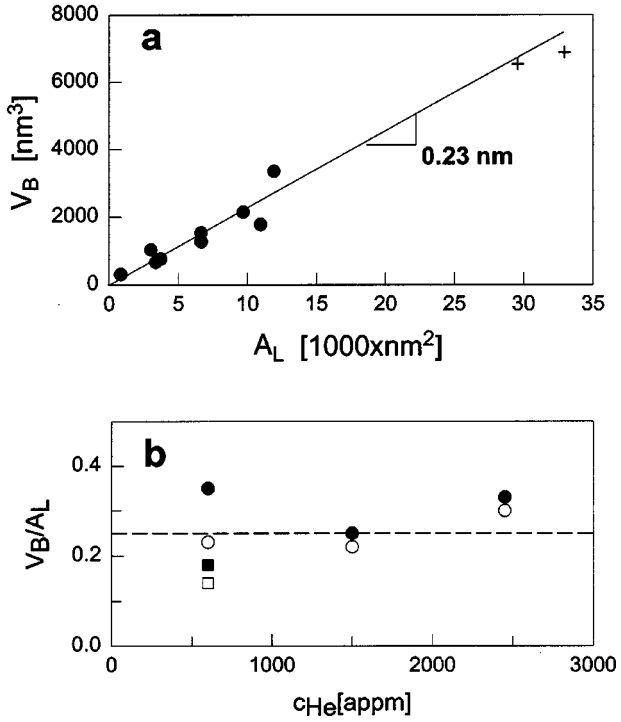

FIG. 11. (a) Volume of bubbles V_A versus area A_L of associated loop (●) or double loop (+) in type-I or-II complexes in 4*H*-SiC implanted to 600 at. ppm and annealed for 1 h at 1720 K. (b) Ratio of total bubble volume to total loop area as a function of He concentration in 4*H*-SiC (solid) and 6*H*-SiC (open) specimens annealed for 1 h at 1620 K (squares) and 1720 K (circles).

With respect to the defects existing in the starting material, namely, GB's, SF's, and dots, the effect of GB's has been described above. SF's had no effect on the formation of defects after implantation and annealing, while the number and size of platelets and bubbles were clearly increasing near dislocations (cf. also Ref. 19). Whether or not the unidentified black and white dots affect nucleation and growth of implantation-induced defects is not clear. Certainly there remained a large number of these defects which were not associated with bubble or loop formation.

IV. DISCUSSION

Specimens irradiated at room temperature with transmitting protons to doses up to 0.2 displacements per atom (dpa) yet without helium implantation show no microstructural changes in TEM, either after irradiation or after subsequent annealing. This means that all microstructural features observed after implantation of SiC are closely related to helium. In the following, the main experimental results, namely, observation of DZ's, appearance of platelets, coarsening of bubbles, and development of loops, will be discussed. The discussion will be partially based on previous results from studies on the behavior of helium and defects in α-SiC.

A. Conclusions from previous studies

(1) Desorption experiments showed that He atoms implanted in α-SiC migrate over macroscopic distances with an activation energy of about 1.1 eV.[20] Extrapolation from this value shows that implanted helium migrates over lattice distances within experimental time scales already at ambient temperature, meaning that trapping at dislocations or GB's is possible, and also clustering of helium atoms if their concentration is sufficiently high. Considering the large number of simultaneously produced vacancies (*V*'s) and their immobility at ambient temperature, the activation energy of 1.1 eV must be ascribed to the dissociation of helium trapped in *V*'s. Consequently, He atoms must be assumed to migrate by the ''dissociative mechanism,'' which is characterized by sequences of trapping, dissociation, and interstitial migration.

(2) Recovery of irradiation-induced strain[21] and thermal conductivity[22,23] in SiC has already started at the irradiation temperature (up to now above room temperature), indicating that at least some defect species are already mobile below ambient temperature. On the other hand, saturation of straining at a relatively high value of about 1% after irradiation around room temperature[24,25] shows that probably not a large fraction of irradiation-induced defects anneal below room temperature, i.e., most self-interstitial atom (SIA's) and *V*'s are immobile up to this temperature or are immobilized by clustering. Furthermore, concurrent recovery of macroscopic strain and lattice-parameter changes in β-SiC indicates that at least for doses up to the onset of saturation (at $\approx$0.1 dpa, i.e., $\approx 7\times10^{25}$ neutrons/m^2) no significant fraction of defects has agglomerated in extended defects by long-range migration.[26] Actually, the recovery of irradiation-induced lattice dilatation shows no dose dependence below $\approx$520 K.[21] This means that, below that temperature, recovery is domi-

nated by correlated recombination, probably mainly of close pairs, while only at higher temperatures can at least one type of defect, probably one type of self-interstitial (C or Si), migrate over larger distances. This is in agreement with the observation of dislocation loop growth only at 900 K.[18] Recovery of irradiation-induced property changes in SiC is practically complete around 1470 K, indicating that at this temperature not only all point defects but also possibly remaining small defect clusters have become mobile.[21]

(3) Diffusion energies of Si and C in α-SiC are in the range of 7–9 eV.[27,28] This means that bulk diffusion of the matrix atoms in SiC can be neglected up to our maximum annealing temperature ($\approx$2020 K). On the other hand, if similar relations between bulk and GB diffusion as in metals are assumed (ratio of GB to bulk self-diffusion energies $\approx\frac{2}{3}$), diffusion of C or Si along GB's or dislocation cores must already be taken into account above 1320 K, which would explain the mobility of clusters in the form of dislocation loops. Apart from this, diffusion along surfaces is expected to be already occurring above about 1000 K.

These results form the framework for the following discussion. Diffusion of He atoms by the dissociative mechanism results in their trapping by extended defects such as dislocations and GB's, and, at sufficiently high concentration, in clustering of interstitial He atoms. Clusters of interstitial He atoms tend to form three-dimensional bubbles; this, however, requires the removal of matrix atoms. This can only occur above about 1400 K, where dislocation core diffusion is expected to become operative. The absence of bubbles in the conventional sense below that temperature and their appearance above it at GB's, dislocations, and in association with dislocation loops inside grains confirm this expectation.

B. Depleted zones

The observation of depleted zones between GB's and the visible defects in the GI, for 2450 at. ppm He even in the as-implanted state, may be explained by the high efficiency of GB's for trapping mobile interstitial He atoms and/or mobile interstitial He clusters, resulting in a reduction of their concentrations in regions adjacent to GB's. There are two mechanisms for the reduction of the cluster density near GB's: (1) He cluster migration to the GB,[29,30] and (2) suppression of cluster nucleation due to a reduction of the He concentration by migration during implantation, and by dissolution of He clusters during annealing.[29,31] Below 1000 K, where neither bulk nor surface self-diffusion takes place, He clusters may safely be considered to be immobile. Furthermore, the first mechanism would yield smooth diffusional cluster/bubble density profiles, whereas the second one would result in sharply defined DZ's,[31] as found in our TEM studies. Assuming that the concentration of solute He is much larger in the GI than at GB's, we expect the width W of the adjacent DZ's to develop with annealing t_a as[29]

$$W^2 - W_0^2 \approx 2\int_0^{t_s} D_{\mathrm{He}}[\hat{c}_{\mathrm{He}}(t)/c_{\mathrm{He}}]dt, \qquad (1)$$

where W_0 is the width of the DZ's after nucleation of stable bubbles during implantation, D_{He} is the He diffusivity, $\hat{c}_{\mathrm{He}}$ is the concentration of interstitial He in solution within the GI, and $c_{\mathrm{He}} \gg \hat{c}_{\mathrm{He}}$ is the implanted He concentration. According to Eq. (1), the growth rate of W^2 should increase with temperature proportionally to the product $D_{\mathrm{He}}\hat{c}_{\mathrm{He}}$, and decrease with the implanted He concentration as $1/c_{\mathrm{He}}$. The growth rate should increase with time as the He concentration in solution $\hat{c}_{\mathrm{He}}(t)$. These predicted trends are qualitatively in agreement with the data in Figs. 2(a)–2(c) but the agreement is far from being quantitative. In particular, the temperature dependence indicated in Fig. 2(a) appears to be much weaker than expected on the basis of a He diffusion energy of 1.1 eV. A quantitative analysis of the parameter dependencies of W is complicated for two reasons: (1) initially submicroscopic He clusters may become visible during annealing, and (2) a possible change in the rate-limiting process may occur,[32] e.g., from resolution of He to recombination of loops. Both these possibilities are suggested by the discussion below.

The widths of DZ's observed in the present work are comparable with widths of DZ's of voids on the order of 1 μm found in metals,[33,34] whereas DZ's of voids in β-SiC (Ref. 18) and B_4C (Ref. 35) are much smaller, which may be explained by the much lower diffusion (and dissociation) coefficients of SIA's and V's as compared to He. DZ's along interfaces are probably the reason why thin fibers in SiC_f/SiC composites are free of irradiation defects as shown in recent experiments.[36]

C. Helium platelets

The plateletlike structures appearing in the GI after implantation of 2450 at. ppm He and at lower He concentrations after subsequent annealing at 1520 K were recently interpreted as He-filled lenticular nanocracks formed by clustering of interstitial He atoms between adjacent (0001) lattice planes.[37] On the basis of this idea, the pressure in the platelets was estimated to reach values of about 24 GPa (see Table II), suggesting that He is solid even at temperatures up to about 470 K. Under such high pressures, circular dislocation dipoles were assumed to form close to the rim of the platelets at a certain critical size. The narrow size distribution and the limitation of growth (see Fig. 4) of the platelets was attributed to their strong elastic binding to the dipoles.

Lenticular cracks or platelets similar to the ones studied in the present work, even though less clear, have been observed previously as compiled in Table II. Some unidentified two-dimensional arrangements have been reported previously for SiC after reactor irradiation which may have produced some He (boron-doped material in a thermal reactor).[4,43,44] In all these cases, the platelets formed parallel to close-packed planes under conditions of missing vacancy supply, while in Si platelet-type structures aligned to (100) planes have been reported.[45]

The concentration of He atoms contained in resolvable plateletlike ''bubbles,'' c_{He}^* (total number of He atoms in bubbles per total number of matrix atoms, which is generally smaller than the concentration of implanted He, $c_{\mathrm{He}}^* < c_{\mathrm{He}}$) may be estimated from the volume fraction occupied by these bubbles, $N_B V_B$, according to

$$c_{\mathrm{He}}^* v_{\mathrm{He}} = \Omega N_B V_B, \qquad (2)$$

TABLE II. Surface energy γ and pressure p of platelets of radius r and half-thickness s, derived from shear moduli μ and Poisson's ratios ν.

	Lattice	μ (GPa)	ν	r (nm)	s (nm)	γ[a] (N/m)	p[a] (GPa)	p/μ	Ref.[b]
SiC	hexagonal	192	0.16	4.5	0.3	3.6	24	0.13	this work
B_4C	trigonal	200	0.14	5	0.25	0.46	3.7	0.019	38
B_4C	trigonal	200	0.14	10	0.1	0.18	3.6	0.018	39
Mo	bcc	125	0.30	5	0.5[c]	7.0[c]	28[c]	0.22[c]	40
Ni	fcc	76	0.31	9	0.5	2.4	9.6	0.13	41
Ti	hcp	45.6	0.36	9	2[c]	25[c]	25[c]	0.55[c]	42

[a]Derived from $p=(\pi/2)[\mu/(1-\nu)](s/r)$ and $\gamma=ps/2$ (Ref. 37).

[b]References for experimental values of r and s.

[c]It is suspected that these values are too high due to experimental errors in s, which may arise from slightly tilting the TEM specimen (Ref. 37).

where N_B and V_B are the number density and the average volume of the bubbles, respectively, v_{He} is the volume per He atom in the bubbles, and $\Omega \approx 10^{-2}\,\mathrm{nm}^3$ is the average volume per atom in the matrix. According to a high-pressure equation of state for He,[46] v_{He} amounts to about $5 \times 10^{-3}\,\mathrm{nm}^3$ at ambient temperature for a pressure of 24 GPa. Treating the platelets as oblate lenticular ellipsoids with diameter and thickness of 9 and 0.6 nm, respectively, we estimate the platelet volume to be about 25 nm^3, containing about 5000 He atoms. $N_B \approx 2\times 10^{21}/\mathrm{m}^3$ gives $c^*_{\mathrm{He}} \approx 100$ at. ppm, which is only about 4% of the implanted He concentration of 2450 at. ppm. Accordingly, most of the implanted He is invisible in TEM and probably most of this is contained in submicroscopic small clusters. The existence of such invisible clusters is confirmed by the increase of the platelet density by about a factor of 2 upon annealing to 1120 K.

D. Formation of bubble-loop complexes

The disintegration of platelets into disks of bubbles and the appearance and growth of interstitial-type dislocation loops attached to them at 1520 K has been recently attributed to a pressure-driven matrix atom transfer from the bubbles to the associated loops by diffusion along bubble surfaces and dislocation cores.[37] This idea is confirmed by a quantitative analysis of the correlation between the total volume of the bubbles V_B and the total area of the loops A_L within individual bubble-loop complexes formed at 1720 K, as shown in Fig. 11(a). Within experimental accuracy, the ratio V_B/A_L corresponds to the separation distance of 0.25 nm of the (0001) planes, meaning that the total number of vacancies in the bubbles equals the total number of matrix atoms (SIA's) in the loops. This correlation also confirms our expectation that, in the temperature range considered here, matrix atoms are not exchanged between complexes by bulk self-diffusion. On the other hand, the strong increase of the total bubble volume in complexes from initially 25 nm^3 for a single platelet to values of 7000 nm^3 for type-III and $>20\,000$ for type-IV complexes indicates the absorption of an enormous amount of He, most of this probably from unresolvable small clusters but perhaps also by resolution of He atoms from small complexes and reabsorption by large ones. The same ratio is obtained when the total bubble volume in a specimen is compared to the total loop area [Fig. 11(b)]. The data for 1620 K are somewhat lower than for 1720 K, which may be due to some error in the determination of very small bubble volumes. On the other hand, at the highest concentration, the very large size and density of loops may have caused some underestimation of the loop area.

Growth of bubbles by removal of matrix atoms results in pressure relaxation and in an increase of v_{He}. At temperatures where bubble-loop complexes form, most of the so far unresolved He may be absorbed by visible bubbles, i.e., $c^*_{\mathrm{He}} \approx c_{\mathrm{He}}$. Certainly, Eq. (2) together with $c^*_{\mathrm{He}} \leqslant c_{\mathrm{He}}$ yields, at a given volume fraction of bubbles $N_B V_B$, a lower-bound estimate for the volume per He atom, v_{He}. For the lowest annealing temperature considered in Fig. 9, 1620 K, we find, with $N_B V_B \approx 4.5\times 10^{-4}$, $v_{\mathrm{He}} \geqslant 8\times 10^{-3}\,\mathrm{nm}^3$, corresponding to a pressure $p \leqslant 20$ GPa at 1620 K,[46] which should be compared to the initial pressure of 24 GPa at ambient temperature and the thermal equilibrium pressure $p = 2\gamma/r \approx 4$ GPa [$\gamma = 3.6$ N/m (Ref. 37)] at 1620 K, where γ is the specific surface free energy and $r \approx 1.5$ nm is the mean bubble radius. According to this, it is clear that the pressure has partially relaxed under these conditions, but is most likely still far above the thermal equilibrium pressure. At higher temperatures, $c^*_{\mathrm{He}} \to c_{\mathrm{He}}$ and $p \to 2\gamma/r$ may be expected. At the highest temperature, 2120 K, these assumptions are, within the experimental accuracy, indeed consistent with the observed bubble structure. Assuming $c^*_{\mathrm{He}} \approx c_{\mathrm{He}}$, we may conclude that the increase in the volume fraction of bubbles with temperature as shown in Fig. 9(a) is mostly due to pressure relaxation and the corresponding increase of v_{He}. Figure 9(c) shows that this relaxation is independent of c_{He}.

E. Correlated bubble-loop coarsening

For the coarsening of precipitates such as bubbles and dislocation loops during annealing, two fundamentally different mechanisms may be distinguished: (1) migration and coalescence of bubbles (MC), and (2) resolution and reabsorption of the atomic constituents, i.e., Ostwald ripening (OR). In the past, only MC (Refs. 29, 46–48) and OR (Refs. 29, 46, 49) of free bubbles not attached to dislocation loops have been considered. For the present study, an apparently pure bubble system is observed only up to 1120 K. At am-

bient temperature, MC of platelet-shaped bubbles may be safely ruled out and even at 1120 K bubble migration by surface diffusion is most likely suppressed by the extremely high pressure in the platelets.[32] A corresponding interpretation of the increase of the platelet density at 1120 K as the result of OR of submicroscopic He clusters, and using for this, e.g., Eq. (10) in Ref. 32 with $r \approx 1$ nm, gives an estimate of the activation energy for He dissociation from such clusters between 3.5 and 4 eV. We expect, however, that the He dissociation energy increases upon pressure relaxation due to the associated decrease of the repulsive energy in the He gas.

At higher temperatures, a detailed analysis of bubble coarsening is difficult for three reasons: (1) inhomogeneity of the bubble distribution and the spatial correlation between bubbles and dislocation loops, (2) strong deviations of the He equation of state from ideal gas behavior at the initially extremely high pressures, and (3) relaxation of these high overpressures to equilibrium during annealing. Because of the latter two effects, the operative coarsening mechanism cannot be identified on the basis of the time dependence of the average bubble size (radius r) since, for initially high pressures, the values of the exponent $n = \partial \ln r / \partial \ln t$ in an assumed power-law dependence of r on time t are expected to be similar for both OR ($n < \frac{1}{2}$) and MC ($n < \frac{1}{3}$),[46,50] i.e., both are in the range of experimental results in Fig. 7(b) ($n \approx 0.17$). Independent of this problem, however, the activation energy E_a of the basic process that is limiting bubble coarsening (atomic diffusion or He dissociation) can be obtained from the values of the exponent n and the effective activation energy E_r of $r(T)$. The experimental data in Figs. 7(a) and 7(b) yield $E_a \approx 4.4 \pm 0.4$ eV for $E_r \approx 0.75$ eV and $n \approx 0.17$ by using the relation $E_a \approx E_r / n$. We mention here that a recent analysis of OR of type-I complexes[51] yields values for n of $\frac{1}{6}$ and $\frac{2}{11}$, depending on specific conditions, i.e., very close to our experimental value (≈ 0.17).

Our observations provide, however, other hints for identifying the coarsening mechanism. (1) The existence of closely spaced bubbles in bubble disks indicates that MC is negligible. (2) Migration would be additionally suppressed by the necessity of nucleation of ledges on the faceted bubbles.[48] (3) Even though some short-range MC within bubble-loop complexes cannot be ruled out completely, long-range migration of individual bubbles out of their native bubble-loop complex or even migration of whole bubble-loop complexes are very unlikely. This follows from the observation that bubbles are only found within complexes where the mutual trapping between bubbles and loops immobilizes these complicated structures. (4) The dependence of bubble size on c_{He}. In MC the average bubble size would increase continuously with c_{He}, whereas in OR it remains constant.[46,52] In spite of the relatively poor experimental accuracy, Fig. 7(c) suggests that the bubble size at least does not increase with c_{He}, thus providing additional evidence for OR as the operative coarsening mechanism.

However, in the present case we are faced with a complex type of OR process: OR of the He bubbles attached to loops requires not only He resolution from and reabsorption by bubbles but also matrix atom transport between bubbles and loops by surface and dislocation core diffusion. The slowest of these processes is rate limiting. Since, the activation energy of 4.4 eV for E_a deduced from our data on the one hand, appears to be higher than our estimate of 3.5–4 eV for the activation energy for He dissociation from clusters under high pressure, and, on the other hand, may be considered to be a reasonable estimate for dislocation core diffusion, we conclude that, at the beginning of pressure relaxation, the latter process is more likely to limit OR of bubbles than He dissociation. A possible change in rate limitation between these two processes by an increase of the He dissociation energy during pressure relaxation could perhaps explain the irregular features in the temperature dependence of DZ's near GB's indicated in Fig. 2(a). Independent of this, OR of bubbles in the temperature range of bubble-loop complexes is closely related to loop coarsening, as expected in view of the correlation between the total bubble volume and the loop area within the complexes. This different type of two-component Ostwald ripening process (migration of He and matrix atoms) is worth studying theoretically in greater detail.

A detailed analysis of the evolution of bubble-loop complexes during annealing (Fig. 10) is difficult because of the occurrence of four different types of complexes. The continuous increase of the loop size with temperature reflects the increasing efficiency of dislocation core diffusion. The complex density does not correspondingly decrease with temperature as expected for a normal coarsening process but increases at the low- and high-temperature sides. Its increase at the low-temperature side is most likely due to OR of submicroscopic He-clusters, whereas the increase at the high-temperature side seems to be associated with the disappearance of multiple-loop complexes. The decrease of the complex density with annealing time as shown in Fig. 10(b) can only be understood by assuming He atom exchange between the complexes by resolution and reabsorption, thus supporting our conclusions above that OR is the operative mechanism. This conclusion is also confirmed by the concentration independence of the complex size in Fig. 10(c).

F. Reasons for different types of bubble-loop complexes

The appearance of the four types of bubble-loop complexes may be interpreted as follows. According to our explanation above of the growth limitation of He platelets by loop formation, we expect loop growth by core diffusion (above 1400 K) to start from these primary loops. Most likely, type I (single bubble with single loop) represents the initial stage in the evolution of the more complicated complexes II to IV. The core of the loop represents a preferential nucleation site for the formation of secondary bubbles under the initially high He supersaturation associated with the high pressure within the still oblate bubbles. Upon disintegration, parts of the primary bubbles may get disconnected from the loop(s) associated with it. Once a bubble has lost its connection to a loop it no longer participates in the OR process and thus stops growing, while bubbles attached to loops will continue to grow. This would explain the formation of type-II and -III complexes. The formation of the interesting type-IV complex seems to require some annealing time and seems to be restricted to lower temperatures and lower He concentrations in the parameter ranges of complexes. At the lower temperatures, core diffusion is still not very efficient. When a certain diffusion length is exceeded upon loop growth, nucleation of a new loop becomes more favorable than further

loop growth. This explains the formation of stacks of loops with a narrow size distribution around 220 nm. With increasing temperature, matrix atoms can be transported along the dislocation core over increasingly longer distances, relaxing the pressure in this way to a level where nucleation of new loops is unlikely to occur. Increasing He concentration seems to have a similar effect, which is probably due to assistance of pressure relaxation by the increasing elastic interaction between the complexes. The prevention of complex formation more complicated than type I along the borders of DZ's is most likely due to drainage of He to GB's, which also assists pressure relaxation.

In the past, stacks of loops or multiple loops of vacancy type have been observed in quenched Al and alloys.[53,54] Interstitial-type multiple loops have so far only been observed under intense electron or ion irradiation, supplying a high supersaturation of interstitials; see Ref. 55. Whether the high supersaturation of interstitials in this case is sufficient for the formation of interstitial-type multiple loops or whether in addition non-inert-gas impurities are needed, is still under debate.[56] Anyhow, these mechanisms are completely different from the present case.

Above 1720 K, the stacks of loops coalesce and form single loops. But even up to 2020 K transport of matter is restricted within the complexes, explaining the observed exact equality of atomic sizes of cavities and associated loops (Fig. 11). Only above 2120 K is this restriction relieved, probably by the beginning of self-diffusion. Loops lose the association with their bubble or bubble disk but are still growing.

V. SUMMARY AND CONCLUSIONS

(1) Helium has a decisive effect on the radiation damage retained in SiC after annealing. A dense population of bubbles and dislocation loops is observed after annealing of helium-implanted SiC, while no visible damage occurs under the same conditions after irradiation without implantation of He.

(2) Damage in helium-implanted SiC after annealing is rather different in three clearly separated locations: grain boundaries, depleted zones along GB's, and the grain interior more than ≈ 0.5 μm away from the GB's. Consequently, no defects were observed in grains smaller than ≈ 0.5 μm.

(3) The DZ's may be beneficial in SiC fibers as long as their diameters are below about twice the width of these zones, i.e., $\leqslant 1$ μm. The DZ's grow upon annealing with a decreasing rate, apparently saturating at values that decrease with increasing helium concentration and seem to be almost independent of annealing temperature.

(4) In SiC implanted to helium concentrations $\geqslant 200$ at.-ppm, faceted bubbles form along GB's during annealing at $\geqslant 1520$ K. This lower-temperature limit slightly decreases with increasing helium concentration.

(5) During helium implantation at room temperature to 2450 at. pppm, platelets of ≈ 9 nm diameter and ≈ 0.6 nm thickness are formed in the matrix on (0001) planes, while at lower concentrations platelets become visible only after annealing around 1520 K.

(6) During annealing at temperatures above 1520 K, in specimens with $\geqslant 350$ at. ppm He, these platelets break up into disks of bubbles, mainly on (0001) planes. The bubbles are faceted with facets on (0001) and $(01\underline{1}2)$ in $4H$-SiC and (0001) and $(01\underline{1}3)$ in $6H$-SiC.

(7) Concurrently interstitial-type dislocation loops are formed, associated in parallel with the bubble disks, with Burgers vectors of $\frac{1}{4}$ and $\frac{1}{6}$ [0001] for $4H$- and $6H$-SiC, respectively. The number of atoms in the loops equals that missing in the associated bubbles within the accuracy of He measurement.

(8) In a parameter window around 1720 K, $c_{\mathrm{He}} \approx 350-600$ at. ppm and $t_a \geqslant 1$ h, stacks of interstitial-type loops form, which transform to single loops at higher temperatures.

(9) Bubbles and loops coarsen upon annealing by apparently strongly correlated coarsening processes.

(10) The formation of He platelets is modeled in terms of clustering of He interstitial atoms between adjacent (0001) lattice planes, thus forming gas-filled nanocracks. The narrow size distribution and the limitation of growth of the platelets are ascribed to their strong elastic binding to circular dislocation dipoles forming close to their rim when they reach a critical size.

(11) The formation of bubble-loop complexes is attributed to pressure-driven matrix atom transfer from the bubbles to the associated loops by dislocation core diffusion.

(12) The coarsening of bubble-loop complexes is described as a two-component Ostwald ripening process in which the processes of He atom exchange between bubbles and matrix atom transfer from bubbles to associated loops are coupled.

ACKNOWLEDGMENTS

The authors are indebted to D. Meertens, V. N. Chernikov (deceased), and T. Schober for their help in interpretation of the TEM results, and to H. Ullmaier for valuable discussions.

[1] K. Hojou and K. Izui, J. Nucl. Mater. **133&134**, 709 (1985).
[2] K. Hojou, S. Furuno, H. Otsu, K. Izui, and T. Tsukamoto, J. Nucl. Mater. **155–157**, 298 (1988).
[3] K. Hojou, S. Furuno, K. N. Kushita, H. Otsu, and K. Izui, J. Nucl. Mater. **191–194**, 583 (1992).
[4] J. C. Corelli, J. Hoole, J. Lazzaro, and C. W. Lee, J. Am. Ceram. Soc. **66**, 529 (1983).
[5] S. H. Harrison and J. C. Corelli, J. Nucl. Mater. **122&123**, 833 (1984).
[6] T. Suzuki, T. Yano, T. Iseki, and T. Mori, J. Am. Ceram. Soc. **73**, 2435 (1990).
[7] T. Suzuki, T. Iseki, T. Mori, and J. H. Evans, J. Nucl. Mater. **170**, 113 (1990).
[8] K. Sasaki, T. Yano, T. Maruyama, and T. Iseki, J. Nucl. Mater. **179–181**, 407 (1991).
[9] T. Suzuki, T. Yano, T. Mori, H. Miyazaki, and T. Iseki, Fusion Technol. **27**, 314 (1995).
[10] P. Jung, Z. Zhu, and J. Chen, J. Nucl. Mater. **251**, 276 (1997).

[11] J. Chen, P. Jung and H. Ullmaier (unpublished).
[12] D. Pandey and P. Krishna, Prog. Cryst. Growth Charact. **7**, 213 (1983).
[13] W. J. Choyke and G. Pensl, MRS Bull. **1997**, 25.
[14] Z. Zhu and P. Jung, J. Nucl. Mater. **212–215**, 1081 (1994).
[15] J. P. Biersack and L. G. Haggmark, Nucl. Instrum. Methods **174**, 257 (1980).
[16] W. Kesternich, in *Proceedings of the 8th European Congress on Electron Microscopy*, edited by A. Csanady, P. Röhlich, and D. Szabo (Programme Community of the 8th European Congress on Electron Microscopy, Budapest, Hungary, 1984), Vol. 2, p. 837.
[17] J. Chen, thesis RWTH Aachen, Forschungszentrum Jülich Report No. Jül-3585, 1998.
[18] R. J. Price, J. Nucl. Mater. **48**, 47 (1973).
[19] K. Nakata, S. Kasahara, S. Shimanuki, Y. Katano, H. Ohno, and J. Kuniya, J. Nucl. Mater. **179–181**, 403 (1991).
[20] P. Jung, J. Nucl. Mater. **191–194**, 377 (1992).
[21] J. Chen, P. Jung, and H. Klein, J. Nucl. Mater. **258–263**, 1803 (1998).
[22] R. P. Thorne, V. C. Howard, and B. Hope, Proc. Brit. Ceram. Soc. **7**, 449 (1967).
[23] M. Rohde, J. Nucl. Mater. **182**, 87 (1991).
[24] R. J. Price, J. Nucl. Mater. **33**, 17 (1969).
[25] R. Blackstone and E. H. Voice, J. Nucl. Mater. **39**, 319 (1971).
[26] H. Miyazaki, T. Suzuki, T. Yano, and T. Iseki, J. Nucl. Sci. Technol. **29**, 656 (1992).
[27] J. D. Hong and R. F. Davis, J. Am. Ceram. Soc. **63**, 546 (1980).
[28] J. D. Hong, R. F. Davis, and D. E. Newbury, J. Mater. Sci. **16**, 2485 (1981).
[29] H. Trinkaus, Radiat. Eff. **101**, 91 (1986).
[30] R. Vaasen, H. Trinkaus, and P. Jung, Phys. Rev. B **44**, 4206 (1991).
[31] R. Vassen, H. Trinkaus, and P. Jung, J. Nucl. Mater. **183**, 1 (1991).
[32] H. Trinkaus, Scr. Metall. **23**, 1773 (1989).
[33] J. O. Stiegler and E. E. Bloom, Radiat. Eff. **8**, 33 (1971).
[34] A. Horsewell, F. A. Rahman, and B. N. Singh, in *Dimensional Stability and Mechanical Behaviour of Irradiated Metals and Alloys* (British Nuclear Energy Society, London, 1983), Vol. 1, p. 69.
[35] A. Jostsons, and C. K. H. DuBose, J. Nucl. Mater. **44**, 91 (1972).
[36] A. Hasegawa, M. Saito, S. Nogami, K. Abe, R. H. Jones, and H. Takahashi, J. Nucl. Mater. **264**, 355 (1999).
[37] J. Chen, P. Jung, and H. Trinkaus, Phys. Rev. Lett. **82**, 2709 (1999).
[38] A. Jostsons, C. K. H. DuBose, G. L. Copeland, and J. O. Stiegler, J. Nucl. Mater. **49**, 136 (1973/74).
[39] T. Stoto, J. Ardonceau, L. Zuppiroli, M. Castiglioni, and B. Weckermann, Radiat. Eff. **105**, 17 (1987).
[40] J. H. Evans, A. van Veen, and L. M. Caspers, Nature (London) **291**, 310 (1981).
[41] M. D'Olieslaeger, L. de Schepper, G. Knuyt, and L. M. Stals, J. Nucl. Mater. **138**, 27 (1986).
[42] T. Schober and H. Trinkaus, Philos. Mag. A **65**, 1235 (1992).
[43] A. M. Carey, F. J. Pineau, C. W. Lee, and J. C. Corelli, J. Nucl. Mater. **103&104**, 789 (1981).
[44] T. Yano and T. Iseki, Philos. Mag. A **62**, 421 (1990).
[45] P. F. P. Fichtner, J. R. Kaschny, R. A. Yankov, A. Mücklich, W. Kreisig, and W. Skorupa, Appl. Phys. Lett. **70**, 732 (1997); and private communications.
[46] H. Trinkaus, Radiat. Eff. **78**, 189 (1983).
[47] E. E. Gruber, J. Appl. Phys. **38**, 243 (1967).
[48] P. J. Goodhew and S. K. Tyler, Proc. R. Soc. London, Ser. A **377**, 151 (1981).
[49] A. J. Markworth, Metall. Trans. A **4**, 2651 (1973).
[50] P. F. P. Fichtner, H. Schroeder, and H. Trinkaus, Acta Metall. Mater. **39**, 1845 (1991).
[51] M. Hartman, Diploma thesis, RWTH Aachen, 1999.
[52] H. Schroeder, P. F. P. Fichtner, and H. Trinkaus, in *Fundamental Aspects of Inert Gases in Solids*, Vol. 279 of *NATO Advanced Study Institute, Series B: Physics*, edited by S. E. Donnelly and J. H. Evans (Plenum, New York, 1991), p. 289.
[53] J. W. Edington and D. R. West, Philos. Mag. **15**, 229 (1967).
[54] A. K. Eikum and D. M. Maher, Phys. Status Solidi A **29**, 281 (1975).
[55] G. Das and T. E. Mitchell, J. Nucl. Mater. **56**, 297 (1975).
[56] L. J. Chen and A. J. Ardell, Phys. Status Solidi A **34**, 679 (1976).